Supporting Information

Lindenmaier et al. 10.1073/pnas.1321883111

SI Text

Instrumentation. ***The Bruker 125HR.*** The Bruker 125HR is a high-resolution solar Fourier transform spectrometer (FTS), specially designed to measure regional atmospheric column composition. It was installed in a region dominated by power plant emissions in March 2011 to make high-precision solar measurements in the near-infrared (NIR) spectral region for emissions verification purposes. Our FTS is part of the Total Carbon Column Observing Network (TCCON; https://tccon-wiki.caltech.edu/; 1, 2), which has stringent protocols for operations, data analysis, and calibration that were established to ensure high accuracy and precision. This section will briefly discuss the main components of the instrument; in-depth descriptions of the instrument, retrieval technique, and error analysis are available at the TCCON website and in ref. 1. The 125HR is equipped with a CaF_2 beam splitter and two detectors at room temperature that simultaneously record the interferograms. The NIR domain (3,800–15,500 cm^{-1}) is observed using InGaAs (3,800–12,000 cm^{-1}) and Si-diode detectors (9,500–30,000 cm^{-1}) in conjunction with a dichroic optic (Omega Optical, 10,000 cm^{-1} cut-on). The NIR interferograms are recorded using an optical path difference of 45 cm with a 2.4 mrad field of view (FOV). This results in an instrument line shape of 0.014 cm^{-1} full-width at half maximum, which is sufficient to fully resolve the individual absorption bands for CO_2, CH_4, CO, N_2O, H_2O, HDO, O_2, and HF.

A solar tracker installed on the roof of the container that hosts the instrument directs the solar beam to the 125HR. This solar beam that has passed through the atmosphere is the light source for our 125HR. The interferograms are collected every 3 min and are used to retrieve the vertically integrated total columns of the atmospheric constituents mentioned above. The GFIT nonlinear least-squares fitting algorithm is used to scale an a priori profile and generate the best spectral fit. The scaled profile is then used to compute the column abundance, which is converted to column-averaged dry-air mole fraction (DMF) for each gas (denoted by X_G) to remove the effects of surface pressure variation. The DMFs are calculated by dividing each gas column by the column of dry air, which is obtained from the O_2 column measured in the same NIR spectrum (1, 2).

When measuring CO_2, TCCON requires high precision and accuracy, otherwise the small gradients in global CO_2 would prohibit in-depth understanding of the carbon cycle. To guarantee this network-wide precision and accuracy, all sites must adhere to TCCON standards of data acquisition and analysis [i.e., they use the same instrument (Bruker 125HR FTS) with identical settings, data acquisition procedures, data processing and analysis software, and calibration onto the World Meteorological Organization's (WMO) gas scale]. The total columns are calibrated based on profiles obtained from aircraft measurements and corrected for systematic errors, including those introduced by omissions in the spectroscopic parameters, spurious air mass dependence, or the modeling of the instrument response (1–3 and references therein). The calibration factor resolves large (~1%) uncertainties in the spectral line parameters and scales the retrievals to the same absolute WMO calibration as the in situ network. The final product is a calibrated column-averaged DMF with a precision better than 0.2% for CO_2 at solar zenith angles (SZAs) smaller than 83°.

Random noise, errors in the a priori profiles, changes in the alignment of the instrument, changes in the performance of the instrument, and surface pressure errors all contribute to this uncertainty. The detailed TCCON procedure for random error calculation is shown by ref. 1 using the perturbation method—that is, each source of error is perturbed by a realistic amount in the GFIT forward model. The fractional difference for each source of error relative to the unperturbed case is then computed, with the total error equal to the sum in quadrature of all individual errors. The average total error for X_{CO2} at the Four Corners site is 0.16% (≤0.9 ppm), which is very close to the results shown for Lamont (1). The X_{CO} total error is 0.66% (≤0.8 ppb).

Pandora complementary metal-oxide–semiconductor spectrometer. The Sun-and-Sky Pandora spectrometer system is a high-precision instrument capable of making column NO_2 measurements within ±0.01 Dobson Units (DU) at a 2min temporal resolution. It is based on an Avantes 50 μm slit spectrometer with a UV sensitive back-thinned 2048 × 64 pixel CCD. Light enters through a single strand multimode optical fiber connected to a sensor head with foreoptics. The lens and fiber optic diameter combine to produce a 1.5° FOV. The sensor head is mounted on a computer-controlled sun tracker and sky scanner (~0.01° pointing precision). The first of two filter wheels contains neutral density filters (ND1, ND2, ND3, and ND4) that allow the 10,000:1 dynamic range necessary for sun and sky observations at all latitudes and seasons. Wavelength calibration and slit functions for the Pandora instruments are determined using precision lasers and lamp emission lines of Hg, Cd, Cu, In, Mg, and Zn, and then validated in the field by analyzing the solar Fraunhofer line structures. Wavelength and radiometric calibration stability are maintained by housing the spectrometer inside an insulated enclosure with internal temperature stabilized to 1 °C using an actively coupled thermoelectric cooler and heater. More detail is provided in ref. 4.

Possible deviations from the actual NO_2 column [$C(NO_2)$] are estimated using a combination of the uncertainties in the relative NO_2 slant column (SCREL), the reference NO_2 slant column (SCREF), and the air mass factor (AMF). The precision of SCREL is approximately ±0.01 DU under clear-sky conditions, but under cloudy skies fewer photons are received during the fixed 20-s integration time, reducing the signal-to-noise ratio and causing the precision to drop to ±0.2 DU. We estimate an additional ±5% uncertainty for SCREL caused by differences between actual and assumed atmospheric temperatures and a similar systematic bias caused by uncertainties in the laboratory absorption cross-sections. On the basis of the field calibration, we estimate the uncertainty of SCREF to be approximately ±0.05 DU, half the stratospheric value of $C(NO_2)$. Uncertainty in the AMF is less than 1% when the SZA is less than 80° and is primarily dependent on assumptions of the height of the effective tropospheric layer, which we have assumed to be 2 km above the local surface. Under clear skies, when the SZA is less than 80°, we can neglect the precision of SCREL and the uncertainty in AMF in the total uncertainty budget, resulting in a simplified estimate of the total uncertainty ER [ER = (±0.05 DU ± 5%)/AMF at the 2-sigma level]. For example, a $C(NO_2)$ measurement of 1.5 DU would have an error estimate of ±0.09 DU for AMF = 1 and ±0.07 DU for AMF = 5.

Picarro gas analyzer. The Picarro G2101-i $^{13}CO_2$ and G2401 CO_2, CO analyzers are based on the Wavelength-Scanned Cavity Ring-Down Spectroscopy technique (5). In brief, a tunable laser is used to rapidly inject light of a specific wavelength into a cavity with a very long optical path length (~20 km). The decay of that light (the ring-down) is dependent on an intrinsic loss of light by the cavity and its mirrors and on absorption by the target gas

molecules. The difference in the decay time for samples with and without target absorbers is proportional to the mole fraction of the target gas. With a tunable laser, multiple species, including isotopic variants, can be scanned in a very short period as long as the spectral features of interest are within a reasonable range. Local air is drawn from a mast at the top of the observatory (~5 m above ground level) at our research facility and delivered to the instruments via insulated 1/4-inch synflex tubing. An automated valve sequencer allows a set of in-house reference gases to be analyzed for the target species of interest (in this case $^{12}CO_2$, $^{13}CO_2$, and CO). The Picarro analyzers have excellent stability, which allows us to limit reference analyses to 20 min every 23 h to check for long-term drift, and any variability that might be attributable to diel influences on system behavior. To date, no significant long-term drift or inconsistencies have been observed, and our independent reference analysis agrees well with the instrument precision reported by Picarro Inc.

$\delta^{13}CO_2 = (R_{sample}/R_{PDB} - 1) \times 1{,}000$ expressed in ‰, where R is the ratio of $^{13}CO_2$ to $^{12}CO_2$ in the sample and reference, the Pee Dee Belemnite being the universally accepted reference (a marine fossil carbonate) for reporting of stable isotope values of carbon. The isotopic CO_2 analyzer reports $\delta^{13}CO_2$ values that are integrated over a 5-min interval with better than ±0.3‰ precision (determined by repeat analyses of the reference gases). The 30-s concentration precision is within 200 ppb for $^{12}CO_2$ and 10 ppb for $^{13}CO_2$. When using the G2401 instrument, the precision of 5-min CO and CO_2 concentrations are better than 2 ppb and 50 ppb, respectively. Please refer to www.picarro.com/products_solutions/scientific_instruments for more information.

The 42i nitrogen oxides analyzer. NO concentration can be determined based on the principle that NO and O_3 react to produce a characteristic luminescence with intensity that is linearly proportional to the NO concentration. The Thermo Fisher Scientific, Inc. 42*i* nitrogen oxides analyzer operates according to this principle to measure NO, NO_2, and NO_x. NO is a straightforward measurement, but NO_2 concentrations are not. NO_2 must be transformed into NO by a molybdenum NO_2-to-NO converter heated to 325 °C, and then the generated NO is measured by the analyzer; the NO_2 concentration in the sample is the difference between the total NO after transformation and the ambient NO. The measurement range for the instrument is 0–100 ppm, with a one-sigma noise value of 0.2 ppb and a 24-h drift that is less than 0.5 ppb. Five-minute data-averaging intervals are used to decrease the noise level and estimated error to less than 0.5 ppb. For more information, please refer to ref. 6.

The 43i sulfur dioxide analyzer. The Thermo Fisher Scientific Inc. 43*i* sulfur dioxide analyzer is a pulsed fluorescence SO_2 analyzer that operates based on the principle that SO_2 molecules absorb UV radiation at specific wavelengths. A sample flows through a fluorescence chamber where pulsating UV light excites the SO_2 molecules. As their energy states decay, these molecules emit UV radiation that is proportional to the SO_2 concentration. A bandpass filter allows only the wavelengths emitted by the excited SO_2 molecules to reach the photomultiplier tube. The instrument measures in the 0–100 ppm range with a lower detectable limit of 0.5 ppb (for data averaged over 5 min) and a 24-h drift that is less than 1 ppb. For more information, please refer to ref. 7.

The WRF-Chem Model. The Weather Research and Forecasting–Chemistry (WRF-Chem) model (8) version 3.1 is used to simulate the chemical and physical behaviors of stack plumes over the complex terrain of the remote sensing verification project (RSVP) site. The 3D, fully compressible, and nonhydrostatic meteorological model is solved on an Arakawa-C grid and terrain-following pressure coordinate system (9). In this study, it is configured with five domains using a one-way nested large-eddy simulation approach. The outermost domain covers the western United States with a horizontal grid spacing of 16.2 km (133 × 107 mesh), whereas the inner nested domains are sequentially zoomed in on the Four Corners region with a nesting ratio of 3. The finest domain encompasses the San Juan and Four Corners power plants (SJPP and FCPP) and the RSVP site. The vertical grids are composed of 60 full-sigma levels stretching from near surface (~28 m at the first half sigma level) to the model top (50 hPa). The first 38 layers are located below 3 km above ground level.

Applied physical processes in the WRF-Chem model include the Goddard shortwave (10) and the Rapid Radiative Transfer Model (RRTM) longwave (11) radiation schemes, the Lin microphysical scheme (12), the Grell–Devenyi ensemble convective scheme (13), the Noah land surface model (14), and the Monin–Obukhov similarity theory (15). Atmospheric boundary layer turbulent mixing is calculated using the Yonsei University nonlocal scheme (16) for domain d01 and d02 and the Mellor–Yamada–Janjic turbulence kinetic energy-based scheme (17) for domain d03 and d04. For domain d05, "effective" turbulence scales are explicitly resolved at the grid scale. The Kinetic PreProcessor method models Regional Atmospheric Chemistry Mechanism gaseous chemistry (18) and the Modal Aerosol Dynamics Model for Europe/Secondary Organic Aerosol Model aerosol (19, 20) processes (21).

Anthropogenic emissions are prepared based on the US Environmental Protection Agency's (EPA) national emission inventory year 2005 for primary pollutants and the Vulcan gridded emissions for CO_2 (www.purdue.edu/eas/carbon/vulcan/), in which the anthropogenic emissions from the SJPP and FCPP were replaced by real-time hourly Continuous Emissions Monitoring System-reported emissions for specific simulation days. Biogenic emissions from natural surfaces are calculated every integration time using the Model of Emissions of Gases and Aerosols from Nature version 2 model (22).

The National Center for Environmental Prediction final analysis global data are used for meteorological initial and boundary conditions of the outermost domain. Initial chemical mixing ratios are obtained from prescribed vertical profiles as in ref. 23 that followed refs. 24 and 25. CO_2 mixing ratios are assigned to 390 ppm homogeneously from the surface to model top. The chemical initial and boundary conditions of nested domain are provided by the simulated chemistry and meteorology in the coarser resolution simulation. Simulations for June 6, 2012 were conducted in this study.

Satellite-Born Instruments for CO_2 and NO_2: An Overview. Although its instrument was not specialized for CO_2 observations, scanning imaging absorption spectrometer for atmospheric chartography (SCIAMACHY) was the first space-born sensor (2002) to show the global distribution of the CO_2 column abundance. Over the past decade, different groups have developed algorithms to analyze the SCIAMACHY spectral observation (26–35) and were able to detect CO_2 variations to within a few ppm—for example, the global annual CO_2 increase of nearly 2 ppm/y and the seasonal cycle of CO_2 over the northern hemisphere (30, 34). Regionally elevated CO_2 was detectable over strong and extended anthropogenic source regions using observations made by SCIAMACHY averaged across several years (34). Although the latest SCIAMACHY CO_2 column abundance retrieval method achieved precisions that were between 1% and 2% with an accuracy of ~1.5% (34), they were still insufficient for flux estimation. SCIAMACHY has also provided extensive NO_2 data that have been used to verify urban and power plant emissions (36).

SCIAMACHY is no longer operational but is succeeded by the Atmospheric Infrared Sounder (AIRS) instrument, which was launched in 2002 onboard NASA's AQUA satellite (37). AIRS is a high-spectral resolution spectrometer that can measure CO_2 in the mid troposphere.

The focus of next-generation satellites is to advance our understanding of natural CO_2 sources and sinks and to verify and constrain anthropogenic emissions. The Japanese Greenhouse Gases Observing Satellite (GOSAT) and the NASA Orbiting Carbon Observatory (OCO) were the first space-based sensors designed specifically to measure CO_2 with the sensitivity, spatial resolution, and geographic coverage needed to quantify CO_2 sources and sinks on regional scales at monthly intervals (38–43).

Placed in a sun-synchronous orbit with an inclination angle of 98 degrees, GOSAT flies at an altitude of ∼666 km and completes an orbit in about 100 min (44–47). The spacecraft flies over the same point on Earth every 3 d. Spectra obtained from the thermal and near infrared sensor for carbon observation (TANSO)-FTS onboard the satellite are used to retrieve column-averaged CO_2 and CH_4 DMF (X_{CO2} and X_{CH4}). TANSO-FTS has a Michelson interferometer that records four spectral bands: 0.758–0.775 μm (12,900–13,200 cm^{-1}) with 0.37 cm^{-1} spectral resolution, 1.56–1.72 μm (5,800–6,400 cm^{-1}), 1.92–2.08 μm (4,800–5,200 cm^{-1}), and 5.56–14.3 μm (700–1,800 cm^{-1}). Bands 2–4 are recorded with 0.26 cm^{-1} spectral resolution. The footprint at nadir of TANSO-FTS has an approximate diameter of 10.5 km at sea level. The nominal single-scan data acquisition time is 4 s. The average total retrieval error for X_{CO2} is 1.48 ppm over land and 1.7 ppm over the ocean (47).

OCO (38) was lost because of a launch vehicle malfunction (48) and was replaced by the OCO-2 mission that is scheduled for launch in July 2014 (http://oco.jpl.nasa.gov/). During its 2-y mission, OCO-2 will fly in a 1:15 PM sun-synchronous orbit with a 16-d ground-track repeat time [preceding the earth observing system (EOS) Aqua platform]. It will have a single onboard instrument that incorporates three high-resolution spectrometers that are designed to measure reflected sunlight in the 0.76 μm O_2 A-band and in the CO_2 bands at 1.61 and 2.06 μm. Each spectrometer will have a 10-km-wide field of view at nadir, which is divided into 1-km-wide samples. The acquisition frequency (4.5 Hz) combined with the spacecraft's ground track speed (6.78 km/s) will result in a down-track resolution at nadir of 1.5 km. A robust validation program was included in the mission to ensure that the space-based X_{CO2} measurements have precisions of ∼0.3% (or 1 ppm) on regional scales (38).

The OCO and GOSAT science teams collaborate closely to develop a common approach for validating their X_{CO2} products. The retrieval method developed originally for NASA's OCO mission was used to calculate the X_{CO2} from spectra recorded by the TANSO-FTS, the new product being named the atmospheric CO_2 observations from space (ACOS) GOSAT X_{CO2} product. Because TCCON has become a reliable source of high-quality ground-based remote sensing measurements of X_{CO2}, detailed comparisons between X_{CO2} retrievals from GOSAT and TCCON have helped to detect and quantify regional-scale biases in the ACOS GOSAT X_{CO2} product. Once in orbit, OCO-2 will deliver high-quality data products (41, 49).

CarbonSat is the European Space Agency's Earth Explorer 8 candidate mission that aims to quantify and monitor CO_2 and CH_4 sources and sinks. Its objective is to better understand the processes that control the carbon cycle dynamics (like GOSAT and OCO) and to estimate the local greenhouse gas emissions in the context of international treaties. To achieve this goal, high spatial resolution of 4 km^2 (2 × 2 km) is coupled with inverse modeling schemes (50). It is anticipated that the instrument will be an imaging grating spectrometer that covers three spectral ranges: 757–775 nm, 1,559–1,675 nm, and 2,043–2,095 nm at a spectral resolution of 0.045, 0.34, and 0.123, respectively. The sun-synchronous orbit altitude is planned at 800 km, with a number of 250 across-track ground pixels and 500 km swath width (lower signal-to-noise ratio than for OCO). The spacecraft will return to observe the same point on Earth every 6 d. The atmospheric CO_2 columns are expected to be retrieved with a precision of 0.5% (2 ppm) or better (50).

The Ozone Monitoring Instrument (OMI) onboard the EOS-Aura satellite, was designed to study the Earth's atmosphere and is capable of detecting global NO_2 concentrations on a daily basis. It is an imaging spectrometer that measures solar radiation backscattered by the Earth's atmosphere and surface. The instrument has two spectrometers: a UV spectrometer that operates in the 270–365 nm range with subranges at 0.42 nm and 0.45 nm resolution and a UV-visible spectrometer that operates in the 350–500 nm range with a resolution of 0.63 nm. The CCD array used by OMI resolves one-dimensional spectral features with a 114° field of view, ensuring a viewing swath transverse to the orbit track of 2,600 km. The instrument's spatial resolution at nadir is dependent on its operational mode but can vary between 13 km × 24 km and 24 km × 48 km (51).

The one-sigma uncertainty for OMI NO_2 retrievals can be estimated as the sum of the AMF uncertainty and the base component from the spectral fitting and stratospheric correction. The base component is dependent on the AMF but ranges between 0.5×10^{15} and 1.5×10^{15} molec·cm^{-2} (52). The relative error is in the 10–40% range, but may include unknown spatial undersampling errors due to a priori (albedo, surface pressure, profile shape) conditions that are only available at resolutions that are coarser than the OMI pixel size (53, 54). OMI retrievals may have larger aerosol error contributions over locations with high aerosol loadings (52).

1. Wunch D, et al. (2011) The Total Carbon Column Observing Network. *Phil Trans R Soc A* 369(1943):2087–2012.
2. Washenfelder RA, et al. (2006) Carbon dioxide column abundances at the Wisconsin Tall Tower site. *J Geophys Res*, 10.1029/2006JD007154.
3. Wunch D, et al. (2010) Calibration of the Total Carbon Column Observing Network using aircraft profile data. *Atmos Meas Tech* 3(5):1351–1362.
4. Herman J, et al. (2009) NO_2 column amounts from ground-based Pandora and MFDOAS spectrometers using direct-sun DOAS technique: Intercomparisons and application to OMI validation. *J Geophys Res*, 10.1029/2009JD011848.
5. Crosson ER (2008) A cavity ring-down analyzer for measuring atmospheric levels of methane, carbon dioxide, and water vapor. *Appl Phys B* 92(3):403–408.
6. Thermo Fisher Scientific Inc (2007) *Model 42i Chemiluminescence NO-NO2-NOx Analyzer, Instruction Manual P/N 101350-00*. www.thermo.com/aqi.
7. Thermo Fisher Scientific Inc (2007) *Model 43i Pulsed Fluorescence SO2 Analyzer, Instruction Manual P/N 101589-00*. www.thermo.com/aqi.
8. Grell GA, et al. (2005) Fully coupled "online" chemistry within the WRF model. *Atmos Environ* 39(37):6957–6975.
9. Skamarock WC, et al. (2008) *A Description of the Advanced Research WRF version 3, Technical Note 475+STR* (National Center for Atmospheric Research, Boulder, CO).
10. Chou M, Suarez MJ (1994) *An Efficient Thermal Infrared Radiation Parameterization for Use in General Circulation Models* (NASA/Goddard Space Flight Center, Greenbelt, MD), NASA Tech Memo 104606 (85).
11. Mlawer EJ, Taubman SJ, Brown PD, Iacono MJ, Clough SA (1997) Radiative transfer for inhomogeneous atmospheres: RRTM, a validated correlated-k model for the long wave. *J Geophys Res* 102(D14):16663–16682.
12. Lin Y, Farley RD, Orville HD (1983) Bulk parameterization of the snow field in a cloud model. *J Clim Appl Met* 22(6):1065–1092.
13. Grell GA, Dévényi D (2002) A generalized approach to parameterizing convection combining ensemble and data assimilation techniques. *Geophys Res Lett* 29(14):38-1–38-4.
14. Chen F, Dudhia J (2001) Coupling an advanced land surface-hydrology model with the Penn State-NCAR MM5 modeling system. Part I: Model implementation and sensitivity. *Mon Weather Rev* 129(4):569–585.
15. Monin A, Obukhov A (1954) Basic laws of turbulent mixing in the surface layer of the atmosphere. *Trudy Geofiz Inst Acad Nauk SSSR* 24(151):163–187.
16. Hong S, Noh Y, Dudhia J (2006) A new vertical diffusion package with an explicit treatment of entrainment processes. *Mon Weather Rev* 134(9):2318–2341.
17. Janjić ZI (2002) *Nonsingular Implementation of the Mellor–Yamada Level 2.5 Scheme in the NCEP Meso Model* (National Center for Environmental Prediction, College Park, MD), NCEP Office Note 437 (61).
18. Stockwell WR, Kirchner F, Kuhn M, Seefeld S (1997) A new mechanism for regional atmospheric chemistry modeling. *J Geophys Res* 102(D22):25847–25879.
19. Ackermann IJ, et al. (1998) Modal aerosol dynamics model for Europe: Development and first applications. *Atmos Environ* 32(17):2981–2999.
20. Schell B, Ackermann IJ, Hass H, Binkowski FS, Ebel A (2001) Modeling the formation of secondary organic aerosol within a comprehensive air quality model system. *J Geophys Res* 106(D22):28275–28293.

21. Damian V, Sandu A, Damian M, Potra F, Carmichael GR (2002) The kinetic preprocessor KPP—A software environment for solving chemical kinetics. *Comput Chem Eng* 26(11):1567–1579.
22. Guenther A, et al. (2006) Estimates of global terrestrial isoprene emissions using MEGAN (Model of Emissions of Gases and Aerosols from Nature). *Atmos Chem Phys* 6(11):3181–3210.
23. Lee S-H, et al. (2011) Modeling ozone plumes observed downwind of New York City over the North Atlantic Ocean during the ICARTT field campaign. *Atmos Chem Phys* 11(14):7375–7397.
24. McKeen S, et al. (2002) Ozone production from Canadian wildfires during June and July of 1995. *J Geophys Res* 107(D14):ACH 7-1–ACH 7-25.
25. Liu S, et al. (1996) Model study of tropospheric trace species distributions during PEM-West A. *J Geophys Res* 101(D1):2073–2085.
26. Buchwitz M, Rozanov VV, Burrows JP (2000a) A correlated-k distribution scheme for overlapping gases suitable for retrieval of atmospheric constituents from moderate resolution radiance measurements in the visible/near-infrared spectral region. *J Geophys Res* 105(D12):15247–15262.
27. Buchwitz M, Rozanov VV, Burrows JP (2000b) A near infrared optimized DOAS method for the fast global retrieval of atmospheric CH_4, CO, CO_2, H_2O, and N_2O total column amounts from SCIAMACHY/ENVISAT-1 nadir radiances. *J Geophys Res* 105(D12): 15231–15246.
28. Buchwitz M, et al. (2005a) Atmospheric methane and carbon dioxide from SCIAMACHY satellite data: Initial comparison with chemistry and transport models. *Atmos Chem Phys* 5(4):941–962.
29. Buchwitz M, et al. (2005b) Carbon monoxide, methane and carbon dioxide columns retrieved from SCIAMACHY by WFM-DOAS: Year 2003 initial data set. *Atmos Chem Phys* 5(12):3313–3329.
30. Buchwitz M (2007) First direct observation of the atmospheric CO_2 year-to-year increase from space. *Atmos Chem Phys* 7(16):4249–4256.
31. Houweling S, et al. (2005) Evidence of systematic errors in SCIAMACHY-observed CO2 due to aerosols. *Atmos Chem Phys* 5(11):3003–3013.
32. Bösch H, et al. (2006) Space-based near-infrared CO2 measurements: Testing the orbiting carbon observatory retrieval algorithm and validation concept using SCIAMACHY observations over Park Falls, Wisconsin. *J Geophys Res*, 10.1029/2006JD007080.
33. Barkley MP, et al. (2007) Assessing the near surface sensitivity of SCIAMACHY atmospheric CO2 retrieved using (FSI) WFM-DOAS. *Atmos Chem Phys* 7(13):3597–3619.
34. Schneising O, et al. (2008) Three years of greenhouse gas column-averaged dry air mole fractions retrieved from satellite–Part 1: Carbon dioxide. *Atmos Chem Phys* 8(14):3827–3853.
35. Schneising O, et al. (2009) Three years of greenhouse gas column-averaged dry air mole fractions retrieved from satellite–Part 2: Methane. *Atmos Chem Phys* 9(2): 443–465.
36. Kim S-W, et al. (2009) NO_2 columns in the western United States observed from space and simulated by a regional chemistry model and their implications for NO_x emissions. *J Geophys Res*, 10.1029/2008JD011343.
37. Barkley MP, Monks PS, Engelen RJ (2006) Comparison of SCIAMACHY and AIRS CO_2 measurements over North America during the summer and autumn of 2003. *Geophys Res Lett*, 10.1029/2006GL026807.
38. Crisp D, et al. (2004) The Orbiting Carbon Observatory (OCO) mission. *Adv Space Res* 34(4):700–709.
39. Crisp D, Miller CE, DeCola PL (2008) NASA Orbiting Carbon Observatory: Measuring the column averaged carbon dioxide mole fraction from space. *J Appl Remote Sens* 2(023508):10.1117/1.2898457.
40. Crisp D (2009) Opportunities for coordinated observations of CO_2 with the Orbiting Carbon Observatory (OCO) and Greenhouse Gases Observing Satellite (GOSAT). *Trans JSASS Space Tech Japan* 7(4):1–43.
41. Crisp D, et al. (2012) The ACOS CO_2 retrieval algorithm–Part II: Global X_{CO2} data characterization. *Atmos Meas Tech* 5(4):687–707.
42. Hamazaki T, Kaneko Y, Kuze A, Kondo K (2005) Fourier transform spectrometer for greenhouse gases observing satellite (GOSAT). *Proc SPIE*, 10.1117/12.581198.
43. Kuze A, Suto H, Nakajima M, Hamazaki T (2009) Thermal and near infrared sensor for carbon observation Fourier transform spectrometer on the Greenhouse Gases Observing Satellite for greenhouse gases monitoring. *Appl Opt* 48(35):6716–6733.
44. Yokota T, et al. (2009) Global concentrations of CO_2 and CH_4 retrieved from GOSAT: First preliminary results. *Scientific Online Letters on the Atmosphere* 5(1):160–163.
45. Butz A, et al. (2011) Toward accurate CO_2 and CH_4 observations from GOSAT. *Geophys Res Lett*, 10.1029/2011GL047888.
46. Morino I, et al. (2011) Preliminary validation of column-averaged volume mixing ratios of carbon dioxide and methane retrieved from GOSAT short-wavelength infrared spectra. *Atmos Meas Tech* 4(6):1061–1076.
47. Yoshida Y (2011) Retrieval algorithm for CO_2 and CH_4 column abundances from short-wavelength infrared spectral observations by the greenhouse gases observing satellite. *Atmos Meas Tech* 4(4):717–734.
48. Palmer PI, Rayner P (2009) Failure to launch. *Nat Geosci* 2(247):10.1038/ngeo495.
49. Wunch D, et al. (2011) A method for evaluating bias in global measurements of CO_2 total columns from space. *Atmos Chem Phys* 11(23):12317–12337.
50. Bovensmann H, et al. (2010) A remote sensing technique for global monitoring of power plant CO_2 emissions from space and related applications. *Atmos Meas Tech* 3(4):781–811.
51. Bucsela EJ, et al. (2006) Algorithm for NO_2 vertical column retrieval from the Ozone Monitoring Instrument. *IEEE Trans Geosci Rem Sens* 44(5):1245–1258.
52. Boersma KF, et al. (2008) Validation of OMI tropospheric NO2 observations during INTEX-B and application to constrain NOx emissions over the eastern United States and Mexico. *Atmos Environ* 42(19):4480–4497.
53. Boersma KF, et al. (2007) Near-real time retrieval of tropospheric NO_2 from OMI. *Atmos Chem Phys* 7(8):2103–2118.
54. Schaub D, et al. (2007) SCIAMACHY tropospheric NO_2 over Switzerland: Estimates of NO_x lifetimes and impact of the complex Alpine topography on the retrieval. *Atmos Chem Phys* 7(23):5971–5987.

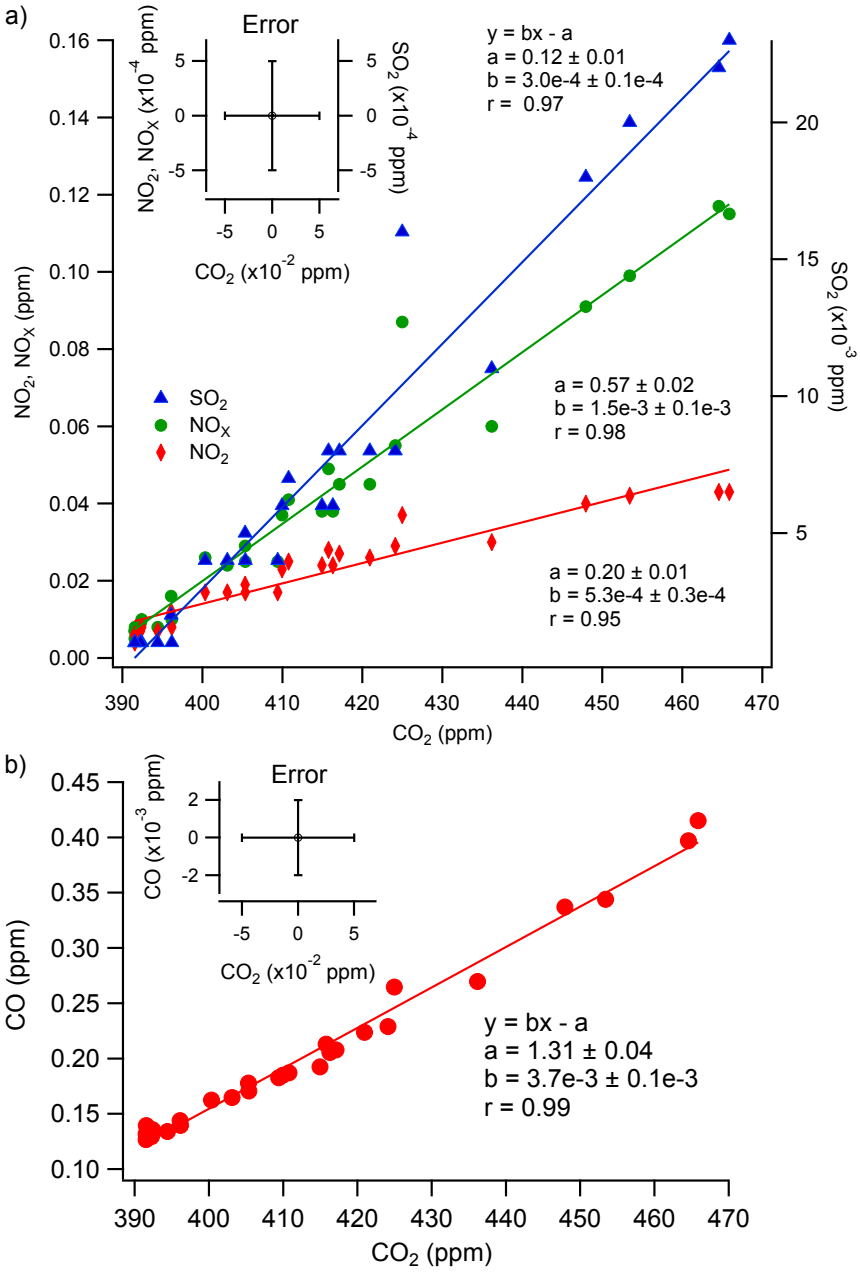

Fig. S1. Correlation plots for (*A*) in situ NO_2 (red diamonds), NO_x (green circles), and SO_2 (blue triangles) versus CO_2 for June 6, 2012. The slopes indicate the emission ratios from the power plants of 5.3×10^{-4} for $\Delta NO_2/\Delta CO_2$, 1.5×10^{-3} for $\Delta NO_x/\Delta CO_2$, and 3.0×10^{-4} for $\Delta SO_2/\Delta CO_2$. These are in strong agreement with the stack emissions from SJPP. The vertical error bar ($\pm 1\sigma$) in the inset indicates the maximum error (5×10^{-4} ppm) for NO_2, NO_x, and SO_2. Similarly, the horizontal error bar shows the maximum error (5×10^{-2} ppm) for CO_2 (*Instrumentation*). (*B*) Correlation plot for in situ CO versus CO_2 for June 6, 2012. The slope of the regression represents the combined urban and forest fire emissions (3.7×10^{-3}). The vertical error bar in the inset indicates the maximum error (2×10^{-3} ppm) for CO, whereas the horizontal error bar shows the maximum error (5×10^{-2} ppm) for CO_2 (*Instrumentation*).

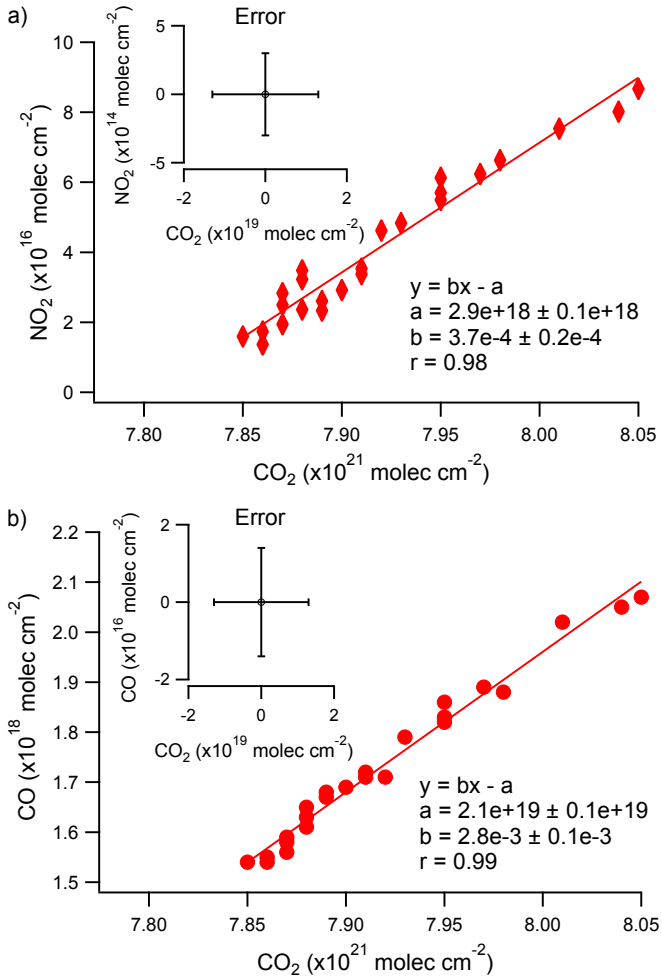

Fig. S2. (*A*) Correlation plot for column NO_2 obtained from the Pandora instrument versus column CO_2 from the 125HR for June 6, 2012. The slope of the regression (3.7×10^{-4}) corresponds to the emission from the SJPP. The inset shows the $\pm 1\sigma$ error for each gas. The vertical error bar shows the maximum error (3×10^{14} molec·cm^{-2}) for NO_2, whereas the horizontal error bar shows the maximum error (1.3×10^{19} molec·cm^{-2}) for CO_2 (*Instrumentation*). (*B*) Correlation plot for column CO versus CO_2 for June 6, 2012. The slope in this case is 2.8×10^{-3}. Again, the inset shows the $\pm 1\sigma$ error for each gas. The vertical error bar shows the maximum error (1.4×10^{16} molec·cm^{-2}) for CO, whereas the horizontal error bar shows the maximum error (1.3×10^{19} molec·cm^{-2}) for CO_2 (*Instrumentation*).

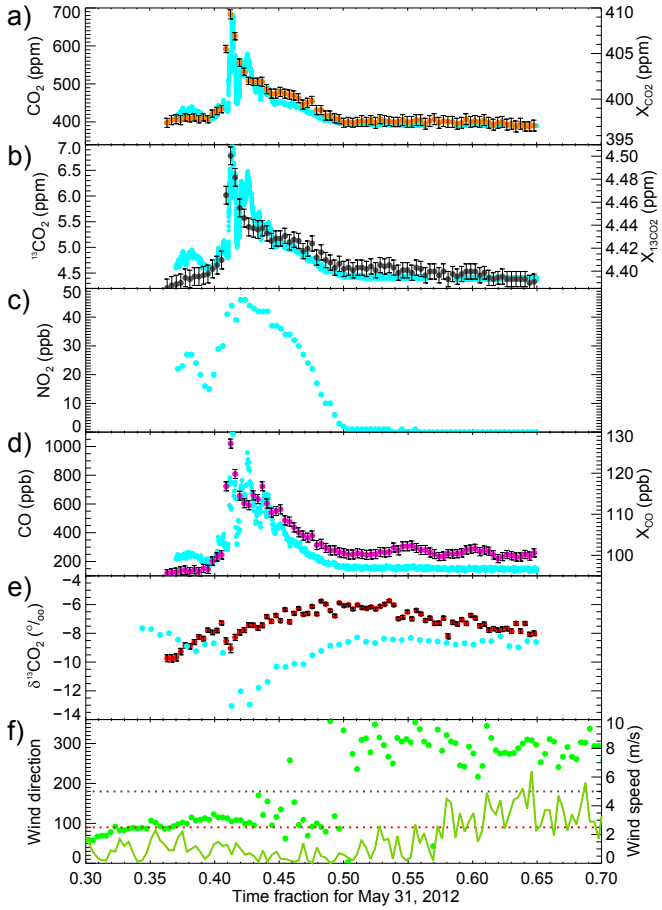

Fig. S3. Observed time evolution of CO_2, $^{13}CO_2$, NO_2, CO, and $\delta^{13}CO_2$ on May 31, 2012. (*A*, *B*, and *D*) 125HR column-averaged DMFs of CO_2 (X_{CO2}, orange), $^{13}CO_2$ (X_{13CO2}, dark gray), and CO (X_{CO}, magenta), respectively, superimposed on the Picarro in situ values of the same gases (cyan). (*C*) EPA in situ (cyan) NO_2 measurements. (*E*) $\delta^{13}CO_2$ (red) calculated from the 125HR measurements smoothed by the empirical function (Eq. **1**), and calculated from the Picarro in situ measurements (cyan). Error bars are indicated for all column results and derived during the retrieval of each gas (*Instrumentation*). For *A*, *B*, and *D*, the primary *y* axis represents the in situ measurements, and the secondary *y* axis represents the column measurements. (*F*) Wind direction (green circles), where 0° corresponds to a wind emanating from the north, 90° from the east (highlighted by the red dotted line), 180° from the south (highlighted by the black dotted line), and 270° from the west. The wind speed is indicated by the solid green line, and its magnitude (in m/s) is reflected in the secondary *y* axis.

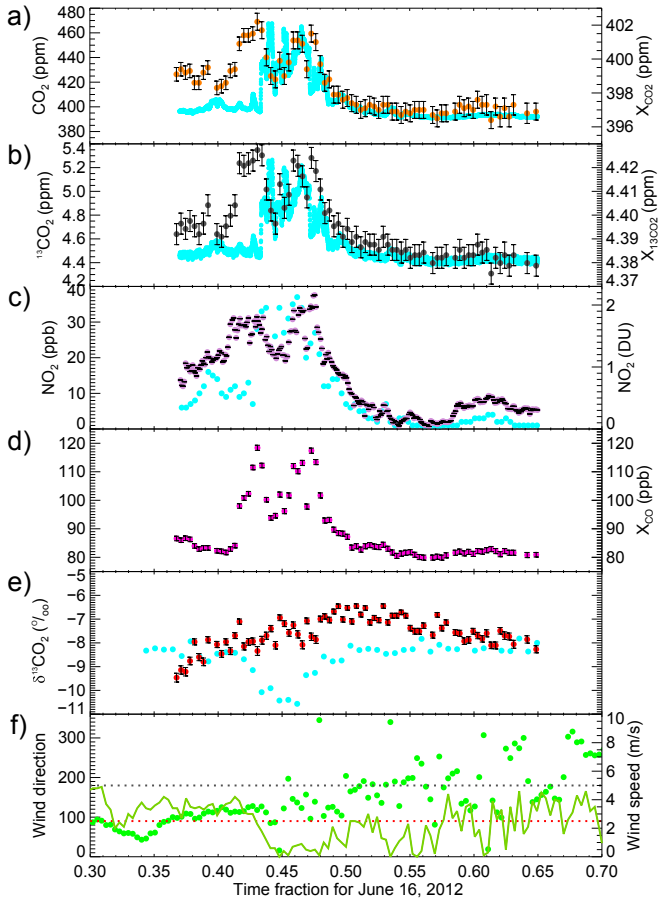

Fig. S4. Observed time evolution of CO_2, $^{13}CO_2$, NO_2, CO, and $\delta^{13}CO_2$ on June 16, 2012. (*A*, *B*, and *D*) 125HR column-averaged DMFs of CO_2 (X_{CO2}, orange), $^{13}CO_2$ (X_{13CO2}, dark gray), and CO (X_{CO}, magenta), respectively, superimposed on the Picarro in situ values (cyan) of the same gases except for CO. (*C*) Pandora (light purple) NO_2 total columns superimposed on the EPA in situ (cyan) NO_2 measurements. (*E*) $\delta^{13}CO_2$ (red) calculated from the 125HR measurements smoothed by the empirical function (Eq. **1**) and calculated from the Picarro in situ measurements (cyan). Error bars are indicated for all column results and derived during the retrieval of each gas (*Instrumentation*). For *A*–*C*, the primary *y* axis represents the in situ measurements, and the secondary *y* axis represents the column measurements. (*F*) Wind direction (green circles), where 0° corresponds to a wind emanating from the north, 90° from the east (highlighted by the red dotted line), 180° from the south (highlighted by the black dotted line), and 270° from the west. The wind speed is indicated by the solid green line, and its magnitude (m/s) is reflected in the secondary *y* axis.

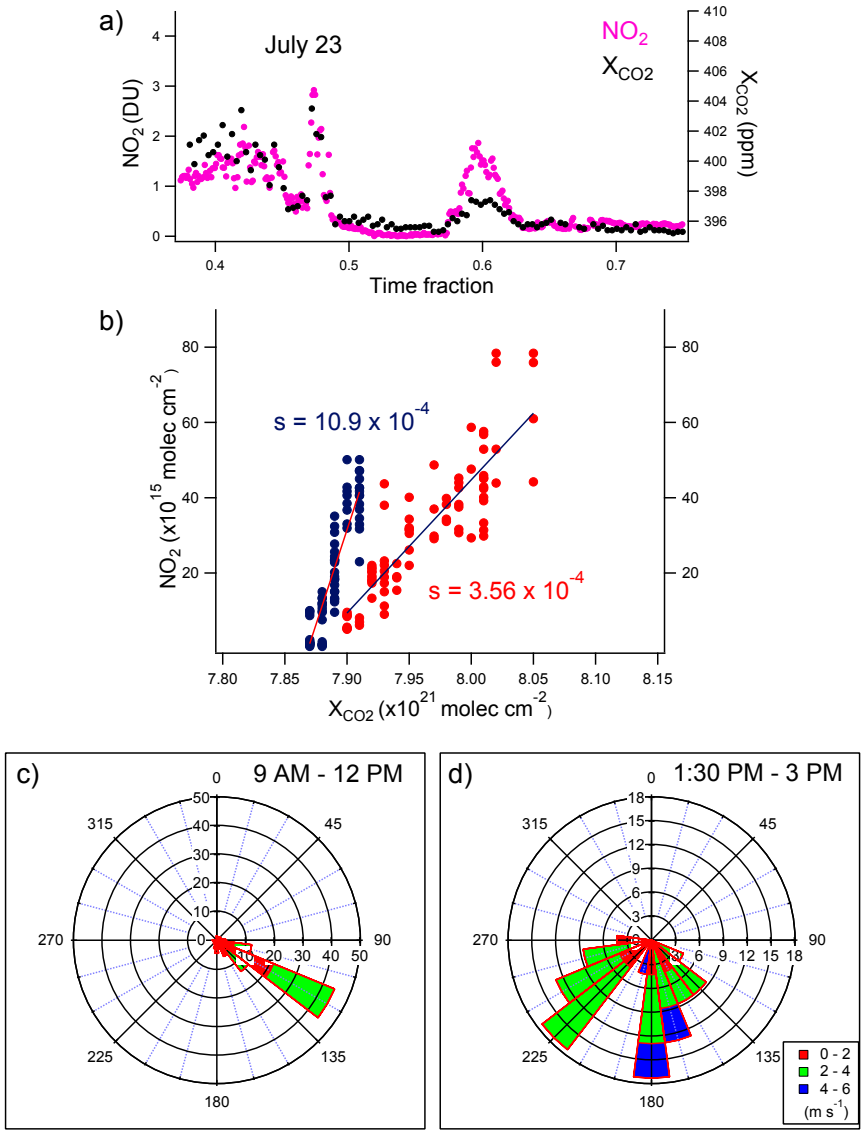

Fig. S5. (*A*) Time series of NO_2 (pink) and CO_2 (black) for July 23, 2013. On this day, two plumes were intercepted by our instruments, one in the morning and one after 1:30 PM (time fraction 0.56). (*B*) NO_2 to CO_2 correlation plot showing that the two plumes belong to different groups. The plume intercepted before local noon belongs to group 2 (red circles), whereas the plume in the afternoon belongs to group 1 (blue circles). The slope of each regression is shown in this panel and represents the emission ratio for each plume. Wind speeds and directions during the periods when the morning plume (*C*) and afternoon plume (*D*) occurred are indicated using rose diagrams. Wind direction is indicated by the petal width using 15° bins and speed by the petal color (red, 0–2 $m{\cdot}s^{-1}$; green, 2–4 $m{\cdot}s^{-1}$; blue, 4–6 $m{\cdot}s^{-1}$). Petal length represents the fraction of time (by percentage) of a plume's duration that a given wind speed–direction combination occurred.

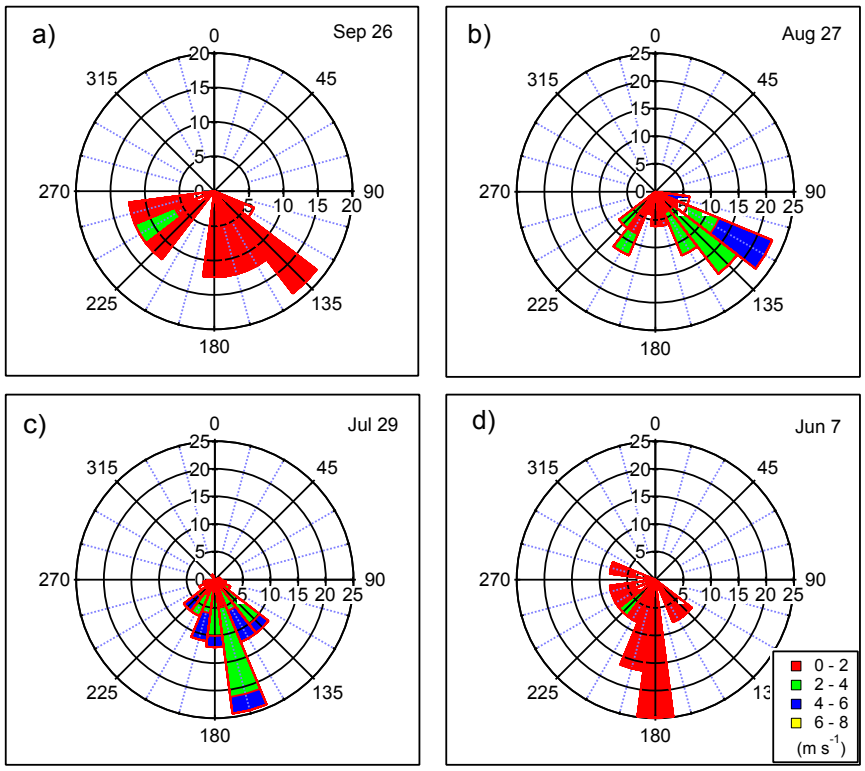

Fig. S6. Wind speeds and directions for group 1 (slope > 5×10^{-4}) on (*A*) September 26, 2012; (*B*) August 27, 2012; (*C*) July 29, 2012; and (*D*) June 7, 2012. Wind direction is indicated by the petal width using 15° bins and speed by the petal color (red, 0–2 $m \cdot s^{-1}$; green, 2–4 $m \cdot s^{-1}$; blue, 4–6 $m \cdot s^{-1}$; yellow, 6–8 $m \cdot s^{-1}$). Petal length represents the fraction of time (by percentage) of a plume's duration that a given wind speed–direction combination occurred.

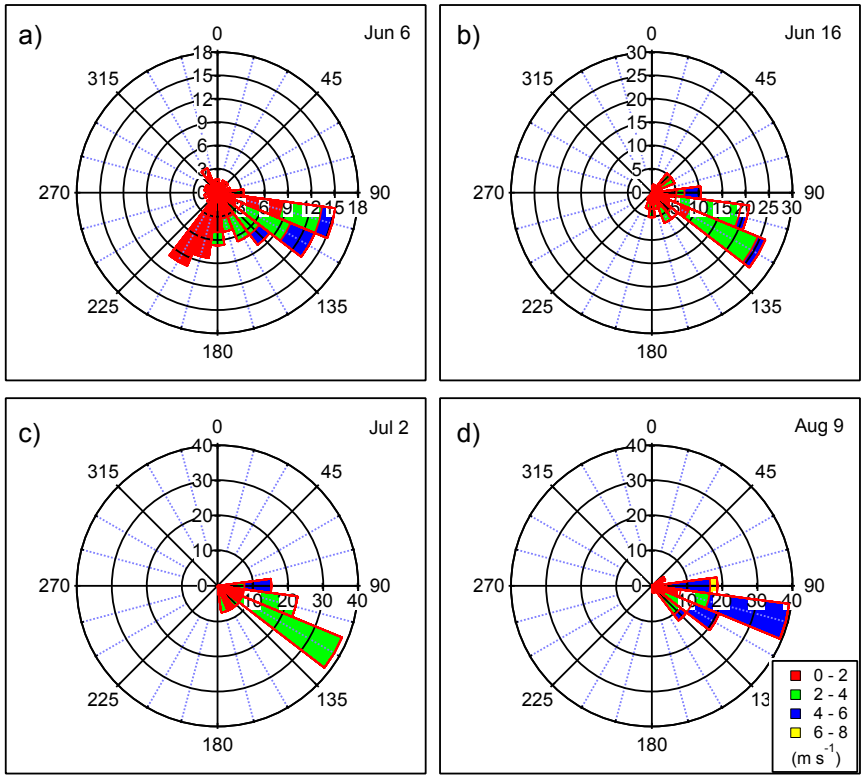

Fig. S7. Wind speeds and directions for group 2 (1×10^{-4} < slope < 5×10^{-4}) on (*A*) June 6, 2012; (*B*) June 16, 2012; (*C*) July 2, 2012; and (*D*) August 9, 2012. Wind direction is indicated by the petal width using 15° bins and speed by the petal color (red, 0–2 $m \cdot s^{-1}$; green, 2–4 $m \cdot s^{-1}$; blue, 4–6 $m \cdot s^{-1}$; yellow, 6–8 $m \cdot s^{-1}$). Petal length represents the fraction of time (by percentage) of a plume's duration that a given wind speed–direction combination occurred.

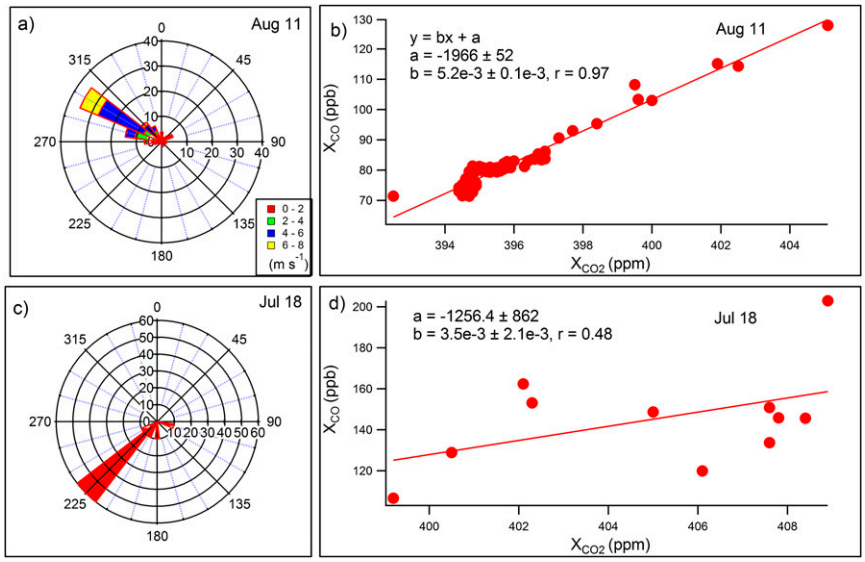

Fig. S8. (*A*) Wind speeds and directions for August 11, 2012, belonging to group 3. Wind direction is indicated by the petal width using 15° bins and speed by the petal color (red, 0–2 $m \cdot s^{-1}$; green, 2–4 $m \cdot s^{-1}$; blue, 4–6 $m \cdot s^{-1}$; yellow, 6–8 $m \cdot s^{-1}$). Petal length represents the fraction of time (by percentage) of a plume's duration that a given wind speed–direction combination occurred. (*B*) X_{CO} versus X_{CO2} correlation is shown for the same plume event. The high emission ratio shown by the slope (5.2×10^{-3}) of the regression indicates incomplete combustion that is common in fires. (*C*) Wind speeds and directions for July 18, 2012. (*D*) X_{CO} versus X_{CO2} correlation is shown for the same plume event. The high emission ratio was 3.5×10^{-3} for this day.

Table S1. NO_x and SO_2 emission ratios calculated from the in situ measurements are compared with the EPA reported emission ratios for groups 1 (blue) and 2 (red), and NO_2 and CO emission ratios calculated from the in situ and column measurements are compared for groups 1 (blue), 2 (red), and 3 (green)

	SJPP	FCPP	in situ (1σ)
$\Delta NO_x/\Delta CO_2$			
September 26	1.27×10^{-3}	2.47×10^{-3}	2.04×10^{-3} (1.38×10^{-5})
August 27	1.21×10^{-3}	2.61×10^{-3}	2.33×10^{-3} (1.58×10^{-5})
July 29	1.28×10^{-3}	2.39×10^{-3}	3.16×10^{-3} (2.14×10^{-5})
June 7	1.25×10^{-3}	2.52×10^{-3}	2.74×10^{-3} (1.86×10^{-5})
May 31	1.43×10^{-3}	2.81×10^{-3}	1.21×10^{-3} (0.82×10^{-5})
June 6	1.53×10^{-3}	2.85×10^{-3}	1.50×10^{-3} (1.02×10^{-5})
June 16	1.39×10^{-3}	2.34×10^{-3}	1.24×10^{-3} (0.84×10^{-5})
$\Delta SO_2/\Delta CO_2$			
September 26	3.48×10^{-4}	5.82×10^{-4}	1.80×10^{-4} (5.61×10^{-6})
August 27	3.67×10^{-4}	5.35×10^{-4}	2.50×10^{-4} (7.79×10^{-6})
July 29	3.06×10^{-4}	5.63×10^{-4}	2.00×10^{-4} (6.24×10^{-6})
June 7	3.61×10^{-4}	5.95×10^{-4}	3.70×10^{-4} (1.15×10^{-5})
May 31	1.97×10^{-4}	3.01×10^{-4}	2.08×10^{-4} (6.48×10^{-6})
June 6	3.16×10^{-4}	3.25×10^{-4}	3.00×10^{-4} (9.35×10^{-6})
June 16	2.17×10^{-4}	3.18×10^{-4}	2.34×10^{-4} (7.29×10^{-6})
	in situ (1σ)	Column (1σ)	col./in situ, % (1σ)
$\Delta NO_2/\Delta CO_2$			
September 26	1.26×10^{-3} (0.85×10^{-5})	9.50×10^{-4} (5.98×10^{-5})	75 (4.7)
August 27	1.64×10^{-3} (1.11×10^{-5})	12.3×10^{-4} (7.75×10^{-5})	75 (4.8)
July 29	1.87×10^{-3} (1.27×10^{-5})	14.0×10^{-4} (8.83×10^{-5})	75 (4.8)
June 7	1.36×10^{-3} (0.92×10^{-5})	8.80×10^{-4} (5.54×10^{-5})	65 (4.1)
May 31	1.60×10^{-4} (1.09×10^{-6})	N/A	N/A
June 6	5.30×10^{-4} (3.59×10^{-6})	3.70×10^{-4} (2.33×10^{-5})	70 (4.4)
June 16	4.90×10^{-4} (3.33×10^{-6})	3.40×10^{-4} (2.14×10^{-5})	69 (4.4)
August 11	0.86×10^{-4} (5.84×10^{-7})	0.43×10^{-4} (2.71×10^{-6})	50 (3.2)
$\Delta CO/\Delta CO_2$			
September 26	N/A	1.01×10^{-3} (8.47×10^{-5})	N/A
August 27	0.62×10^{-3} (6.37×10^{-6})	0.56×10^{-3} (4.69×10^{-5})	90 (7.5)
July 29	N/A	0.31×10^{-3} (2.59×10^{-5})	N/A
June 7	0.78×10^{-3} (8.01×10^{-6})	0.74×10^{-3} (6.20×10^{-5})	94 (7.9)
May 31	3.39×10^{-3} (0.35×10^{-5})	2.57×10^{-3} (2.15×10^{-4})	76 (6.4)
June 6	3.65×10^{-3} (0.37×10^{-5})	2.82×10^{-3} (2.36×10^{-4})	77 (6.4)
June 16	N/A	6.64×10^{-3} (5.56×10^{-4})	N/A
August 11	9.69×10^{-3} (9.9×10^{-5})	5.17×10^{-3} (4.33×10^{-4})	53 (5.0)

The in situ emission ratios are followed by SD (1σ). The EPA does not provide errors for the reported emissions. The numbers in parentheses represent the SD (1σ).